PCCP

ARTICLE

Effect of crystallinity on photocatalytic performance of Co₃O₄ water-splitting cocatalyst †

Chin Sheng Chua,[a] Davide Ansovini,[a,b] Coryl Jing Jun Lee,[a] Yin Ting Teng,[d] Lay Ting Ong,[a] Dongzhi Chi,[a] T. S. Andy Hor,[a,c] Robert Raja,[b] and Yee-Fun Lim,[a]*

Cocatalysts, when loaded onto a water splitting photocatalyst, accelerate the gas evolution reaction and improve the efficiency of the photocatalyst. In this paper, we report that the efficiency of the photocatalyst is enhanced with an amorphous cobalt oxide cocatalyst. WO_3 film, when loaded with amorphous or nanocrystalline Co_3O_4, shows an improvement of up to 40% in photocurrent generation and 34% in hydrogen gas evolution. The effect of cocatalyst crystallinity on performance was systematically studied, and we found that the photocurrent deteriorates with the conversion of the cocatalyst to highly crystalline phase at annealing temperature of 500 °C. The mechanism for this effect was studied in detail using electrochemical impedance spectroscopy, and the enhancement effect produced by amorphous cocatalyst is attributed to the large density of unsaturated catalytically active sites in the amorphous material.

1. Introduction

Photocatalytic water splitting is an attractive process as it produces energy from a clean process starting from renewable raw materials and stores this energy in the form of hydrogen gas.[1] The process involves (i) absorption of photons and generation of electron-hole pair, (ii) separation and migration of electron-hole pair, and (iii) surface redox reaction via photogenerated electrons and holes. For water splitting, the surface redox reaction is a combination of two half-reactions, hydrogen evolution reaction (HER) and the oxygen evolution reaction (OER).[2] Of the two half-reactions, OER is more complex as it requires multiple interactions and the removal of four protons and electrons for oxygen to evolve.[3] As such, much work had focused on improving the solar-to-oxygen conversion efficiency for photoanode catalysts.

Photoanode materials used for OER are n-type semiconductors whose band bending at the surface drives minority holes to its surface. Among the various n-type semiconductors, tungsten oxide (WO_3) has been widely studied due to its good stability in neutral to acidic solution,[4] non-toxicity, good charge transport properties[5] and high oxidation power of valence band holes (+3.1–3.2 V vs normal

hydrogen electrode (NHE)).[6] Its bandgap of 2.6-2.8 eV allows absorption of the blue portion of the visible spectrum. While it has a theoretical solar-to-hydrogen efficiency of ca. 4.5%,[5] such efficiency is rarely attained due to losses such as recombination of charge carriers and kinetic loss.[7] To reduce these losses, the photocatalyst can be loaded with cocatalysts which improve the efficiency of the water splitting process.

When loaded by a proper amount (typically <5%), cocatalysts help to accelerate the water splitting reaction with a photocatalyst. The deposited cocatalyst serves as reaction sites for the water splitting process and catalyses the reaction.[8] They also promote the transportation of charges from the catalyst, and increase charge separation at the interface between cocatalyst and the photocatalytic semiconductor.[9] In addition, the cocatalyst improves the stability of the photoanodes by extracting photogenerated holes from the photoanodes, thus suppressing photocorrosion.[10] For HER, platinum (Pt) is usually considered as the best cocatalyst. A volcano relation had been established between the exchange current for H_2 evolution and the bond strength of metal-hydrogen, and Pt sits at the peak of the volcano.[11] In the case of OER, a clear dominant cocatalyst has yet to be established. Several inorganic cocatalysts, such as IrO_x,[12] CoO_x,[10] Co_3O_4,[13] NiO_x,[9, 13] and RuO_2,[14] were found to enhance the photocatalytic reaction.

While it may be expected that highly crystalline cocatalysts would show good performance due to favourable charge transport properties, some of the most effective cocatalysts that have been reported were amorphous materials such as MoS_2,[15] CoO_x[16] and Co-Pi.[17, 18] The effect of the crystallinity on the performance of these cocatalysts, however, has not been systematically studied. In this work, we investigated the effect of the crystallinity of Co_3O_4 cocatalysts on the photocatalytic

a. Institute of Materials Research and Engineering (IMRE), A*STAR (Agency for Science, Technology and Research), 3 Research Link, Singapore 117602, Singapore. Email: limyf@imre.a-star.edu.sg
b. School of Chemistry, University of Southampton, Highfield, Southampton SO17 1BJ, United Kingdom.
c. Department of Chemistry, National University of Singapore, 3 Science Drive 3, Singapore 117543, Singapore
d. Energy Research Institute @NTU (ERI@N), Research Techno Plaza, X-Frontier Block, Level 5, 50 Nanyang Drive, Singapore 637553, Singapore
† Electronic Supplementary Information (ESI) available: Additional XRD, XPS, EIS data. See DOI: 10.1039/x0xx00000x

water splitting performance of WO$_3$ film. The cocatalyst and WO$_3$ photocatalyst film were deposited using sol-gel processing. Sol-gel deposition is a low-cost solution-based method, and offers distinct advantages such as large area film deposition and ease of control over the film's stoichiometry.[19, 20] Here, we will report the photoelectrochemical (PEC) analysis and gas evolution performance of the Co$_3$O$_4$/WO$_3$ films. The superior photocurrent generation capability of amorphous cocatalyst compared to their crystalline counterpart will also be presented, together with a detailed mechanistic study of this effect based on electrochemical impedance spectroscopy (EIS).

2. Experimental

2.1 Synthesis of WO$_3$ sol-gel precursor solution

The deposition of WO$_3$ thin film was carried out by spin-coating WO$_3$ sol-gel precursor solution onto fluorine-doped tin oxide (FTO) coated glass. The WO$_3$ precursor solution was prepared by first adding 0.4 ml of acetylacetone into 5 ml of methanol, after which the solution mixture was slowly added into 0.5 g of WCl$_6$ (Sigma Aldrich) before undergoing further dilution with 5 ml of methanol. 0.25 g of poly(ethylene glycol) (Sigma Aldrich, average molecular weight of 200) was then added to the solution to improve the film quality during spin-coating. The solution was allowed to age under constant stirring for 4 days before use. All of the above steps were carried out inside a nitrogen-filled glovebox.

2.2 Thin film deposition

Prior to the spin-coating process, the substrates were cleaned by sonication in ethanol for 5 minutes followed by oxygen plasma treatment with Trion Sirus reactive ion etcher at 100 W for 2 minutes. The sol-gel solution was pre-filtered with a 0.45 µm PVDF Whatman syringe filter, and then spin-coated onto the substrate at 2000 rpm for 30 seconds. After each spin-coating cycle, the substrates were annealed at 300 °C for 2 minutes to convert the organic layer into oxide. The process was repeated for 20 cycles to obtain a WO$_3$ film with a final thickness of about 1.4 µm. To obtain crystalline WO$_3$ film, the substrates were subjected to a final annealing step at 500 °C for 1 hour.

Co$_3$O$_4$ was deposited on WO$_3$ through sol-gel spin-coating. Its precursor solution is prepared by mixing 0.05 g of cobalt acetylacetonate into 10 ml of methanol with 0.1 ml of ethanolamine as a stabilizer. The precursor solution is stirred overnight before spin-coating onto the WO$_3$ film using the same spin parameters as that for WO$_3$. The cocatalyst solution was spin-coated for 1 cycle followed by annealing on a hotplate for 15 minutes. For comparison purposes, WO$_3$ samples loaded with NiO$_x$ cocatalysts were also prepared; the NiO$_x$ was deposited from a nickel acetate precursor solution of similar concentration.

2.3 Structural characterization

X-ray diffraction (XRD) spectra of the deposited films were analysed using Bruker D8 general area detector diffraction system (GADDS). Film morphology was characterized using ESM-9000 field-emission scanning electron microscope (FE-SEM). X-ray photoelectron spectroscopy (XPS) was carried out with VG Thermo ESCALab 220i-XL X-ray photoelectron spectrometer using monochromatic Al Kα (1486.6 eV) as the X-ray source. The binding energies were charge corrected using adventitious C 1s peak at 285.0 eV as a reference. UV-Vis absorbance studies were carried out using Shimadzu 3101 UV-VIS-NIR spectrophotometer.

2.4 PEC measurement

Photoelectrochemical (PEC) measurements were carried out in a 3-electrode configuration using Ag/AgCl reference electrode, Pt counter electrode and the cocatalyst/WO$_3$ film coated on FTO glass as the working electrode. A black tape was used to define the active area of 1 cm^2 on the coated sample. The electrodes were immersed inside a 0.1 M Na$_2$SO$_4$ aqueous electrolyte solution, with a pH of 5.84 as measured by a Hanna Instruments pH meter. The PEC measurement was carried out using Metrohm Autolab PGSTAT101 potentiostat. The light source used was an Oriel solar simulator using a 150 W Xenon arc lamp fitted with an AM 1.5 filter, with light intensity maintained at 100 mWcm^{-2}. Using Metrohm Autolab PGSTAT302N potentiostat, electrochemical impedance spectroscopy (EIS) data was collected with an amplitude setting of 10 mV and frequency varying from 0.1 to 100,000 Hz. The electrolyte used is 0.1 M Na$_2$SO$_4$ solution and at a potential of 1.2 V vs Ag/AgCl.

2.5 Gas evolution analysis

Photoelectrocatalytic water splitting gas evolution was characterized in a closed recirculating glass reactor filled with Ar gas. The same 3-electrode configuration and electrolyte solution was used for the gas evolution measurement. The electrodes were connected to DY2100 series potentiostat (Digi-Ivy, Inc.), which was used to supply a constant voltage of 1 V across the reference and working electrode. The samples were illuminated with a 150 W Xenon arc lamp fitted with AM 1.5 filter at a light intensity of 50 mWcm^{-2}. The amount of evolved gases was analysed by gas chromatography (Shimadzu, GC-2014 with TCD detector and MS-5A column, Ar carrier).

3. Results and discussion

XRD spectra of the deposited WO$_3$ film on FTO glass and thick Co$_3$O$_4$ film on silicon substrate are shown in Figure 1. The WO$_3$ film shows distinct peaks at 2θ = 24.8°, 34.6°, and 50.3°, which matches well with the data from JCPDS 01-083-0950 (monoclinic WO$_3$ crystal structure). Crystalline Co$_3$O$_4$ film annealed at 500 °C show single crystalline phase with peaks consistent with the corresponding literature data in the JCPDS database (00-043-1003 and 01-078-0429 respectively). Thus,
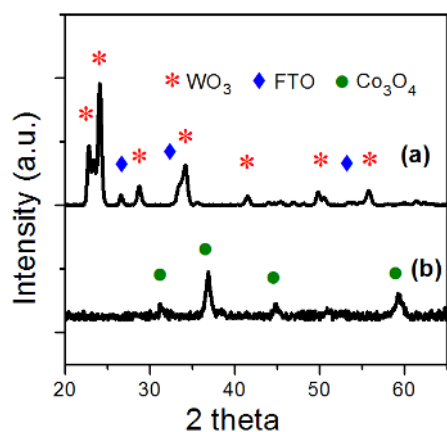
ARTICLE

Figure 1 XRD pattern of (a) WO_3 film on FTO glass annealed at 500 °C and (b) Co_3O_4 on silicon annealed at 500 °C.
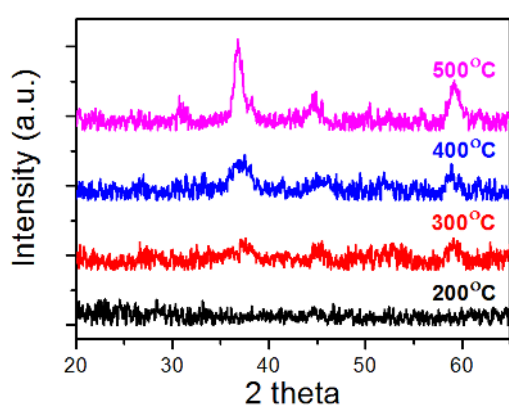

Figure 2 Evolution of XRD pattern of Co_3O_4 film on silicon at different annealing temperatures.

the XRD data confirmed that the desired oxide materials have been obtained from the sol-gel process. In addition, the deposition of an ultra-thin layer of Co_3O_4 cocatalyst film on WO_3 did not result in any crystallinity change for the WO_3 film (Figure S1 in the ESI). Figure 2 shows the evolution of the XRD spectra of Co_3O_4 film at different annealing temperature. From the XRD spectra, it can be seen that the Co_3O_4 film is completely amorphous at 200 °C, while a nano-crystalline phase starts to emerge at 300 and 400 °C. At 500 °C, highly crystalline Co_3O_4 phase can be observed from the XRD pattern. Using Scherrrer equation, the crystallite size of Co_3O_4 increases from 3.7 nm (at 400 °C) to 7.8 nm (at 500 °C).

The optical absorption properties of WO_3 and Co_3O_4/WO_3 film are shown in Figure 3. Figure 3a shows that WO_3 film absorbs photons in the UV spectrum with its absorption edge at about 450 nm. With an ultra-thin layer of Co_3O_4, there is a very slight increase in absorbance at wavelengths up to around 600 nm. This is due to the smaller bandgap of Co_3O_4, previously reported to be 2.07 eV.[21] From the absorbance data, a Tauc plot is generated for WO_3 film using the following equations:

$$\alpha = 2.302\, A/t \qquad (1)$$
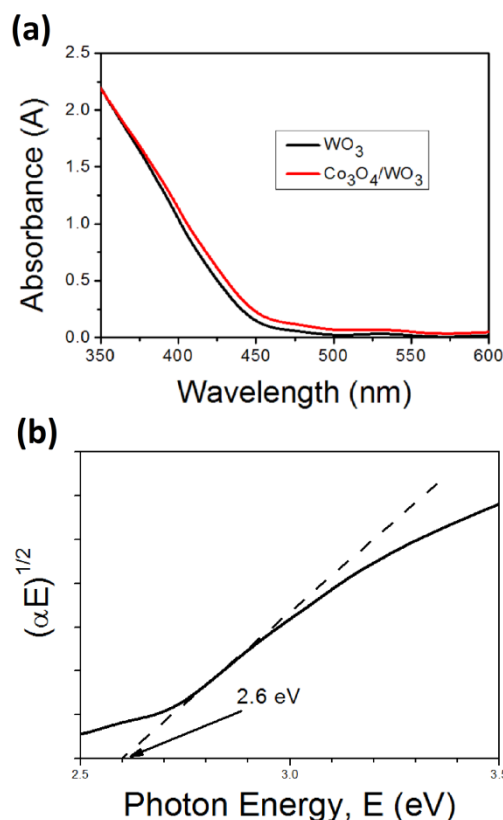
$$(\alpha E)^{\gamma} \propto (E - E_g) \qquad (2)$$

Figure 3 (a) UV-Vis absorption spectra of WO_3 and Co_3O_4/WO_3 film. (b) Tauc plot and band gap determination of WO_3 film.

where α is the absorption coefficient, A is the film absorbance, E is the photon energy, E_g is the band gap and the exponential γ equals to 0.5 for indirect band gap material. With the Tauc plot, the band gap of the deposited WO_3 film is determined to be 2.6 eV which is similar to reported works in the literature.[22]

Morphology of the deposited WO_3 and Co_3O_4/WO_3 thin films can be seen from the SEM images shown in Figure 4. The sol-gel deposited WO_3 film shows a porous structure with some short interconnecting rods of WO_3 particles connecting between different growth regions on the film. With an ultra-thin layer of Co_3O_4 deposited on top, little change in the film morphology is observed. Cross-sectional SEM image (Figure S2 in the ESI) shows only the WO_3 layer (with a thickness of around 1.4 μm), while the Co_3O_4 layer is unobservable. Further analysis using energy dispersive X-ray (EDX) (Figure S3 in the ESI) could not detect any cobalt ions from the cocatalyst layer, and only tungsten and tin (from the FTO layer) ions showed up in the spectrum.

As XRD, SEM and EDX analysis could not detect the presence of the ultra-thin layer of Co_3O_4 cocatalyst, further analysis was performed using XPS. Figure 5 shows the XPS data for a Co_3O_4/WO_3 thin film sample with the cocatalyst annealed to 350 °C. The Co 2p spectra consist of two main peaks at 797.1 and 781.2 eV, which corresponds to Co 2p$^{1/2}$ and 2p$^{3/2}$ binding energies respectively and confirms the presence of Co on the surface. Our value for the Co 2p$^{3/2}$ binding energy is slightly higher than the typically reported range of 780.0-780.9 eV.[23, 24] It is known that the 2 cobalt oxidation states
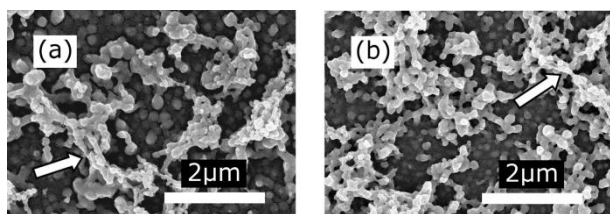
Figure 4 Surface morphology of (a) WO_3 film, and (b) Co_3O_4/WO_3 film. The arrows point to the short interconnecting rods between growth regions.
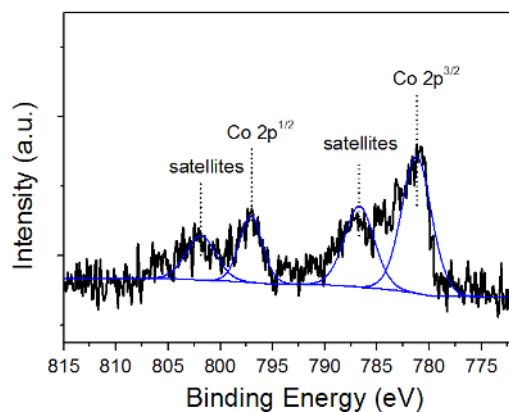

Figure 6 Photocurrent densities of bare WO_3, 1 layer and 3 layers of Co_3O_4 on WO_3 (annealed at 350 °C).

Figure 5 XPS spectra of Co 2p for Co_3O_4/WO_3 film with the cocatalyst annealed at 350 °C.

Figure 7 Percentage change in photocurrent (with respect to bare WO_3) with cocatalyst annealing temperature for Co_3O_4/WO_3 film at 1.2 V vs Ag/AgCl.

present in Co_3O_4, namely Co^{3+} and Co^{2+}, have binding energies of 780 and 782 eV respectively.[24] Thus, the slightly higher binding energy observed for our sample may be indicative of a larger percentage of Co^{2+} ions. The other two peaks at 803.1 and 787.1 eV can be attributed to its shake up satellite peaks.[25]

To investigate the photocurrent generation capabilities of WO_3 and Co_3O_4/WO_3, linear sweep voltammetry was utilized under dark and light condition using Ag/AgCl as the reference electrode. Figure 6 shows the PEC current-voltage curve of bare WO_3 and Co_3O_4/WO_3 film. Under dark condition, all the deposited films show negligible current flowing through the system, as can be observed for WO_3 film in the dark. With AM 1.5 illumination, WO_3 film shows a measured photocurrent of 0.42 mAcm^{-2} at 1.2V (vs Ag/AgCl). This is comparable to WO_3 films deposited with other synthetic methods[26] but lower than nanostructured films with high surface area.[27] With a layer of cocatalyst deposited, the WO_3 film shows an almost 40% increase in photocurrent generation. The results show that the Co_3O_4 is effective in improving the photoactivity of the WO_3 film. The amount of cocatalyst can be controlled by varying the cocatalyst thickness, which is determined by the number of spin-coated layers. A thicker cocatalyst layer, however, have a deteriorative effect as can be seen with 3 layers of Co_3O_4 film. The decrease in photocurrent is due to better coverage of the 3 layer coating which blocks the active sites in the WO_3 film.[28]

Figure 7 presents the change in photocurrent with annealing temperature of the cocatalyst. The photocurrent shows an initial increase with annealing temperature before deteriorating at annealing temperature of more than 400 °C.
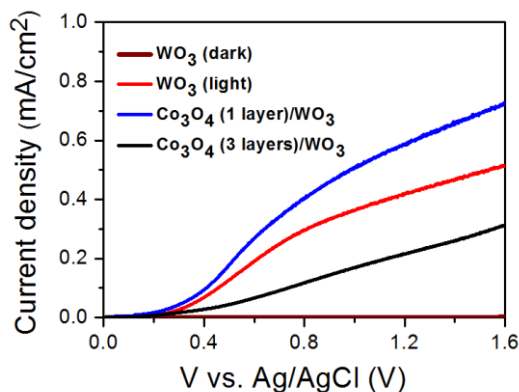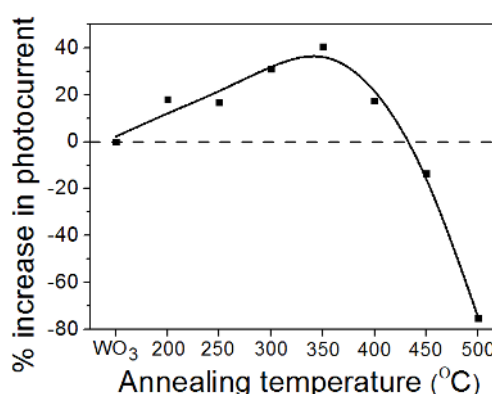
The deterioration in photocurrent may be attributed to the increasing crystallinity of the cocatalyst film at higher annealing temperatures. In order to verify if this effect is also observable for other cocatalysts, a similar study was performed on WO_3 films loaded with NiO_x. The same trend was observed with the NiO_x cocatalyst, whereby amorphous or nanocrystalline cocatalysts annealed below 400 °C outperform highly crystalline cocatalysts annealed at higher temperatures (Figures S4-S6 in the ESI).

A systematic mechanistic study of the above-mentioned effects was performed using electrochemical impedance spectroscopy (EIS). Figure 8 shows the EIS data of Co_3O_4 cocatalyst deposited on WO_3 film under light illumination. The EIS Nyquist plot consist of 2 semi-circles, with the high frequency arc (first semicircle) corresponding to the fast charge transport through the WO_3 and cocatalyst film (R_{Bulk} and CPE_{Bulk}) and the low frequency arc (second semicircle) corresponding to the slower interfacial charge transfer at the film-electrolyte interface (R_{CT} and CPE_{CT}).[29] Using the model in Figure 8b for equivalent circuit fitting, the values for R_{Bulk}, CPE_{Bulk}, R_{CT}, and CPE_{CT} are obtained and shown in Table 1.

At low cocatalyst annealing temperature (< 400 °C), the value of the charge transfer resistance (R_{CT}) is found to be lower for the cocatalyst/WO_3 films compared to bare WO_3. The

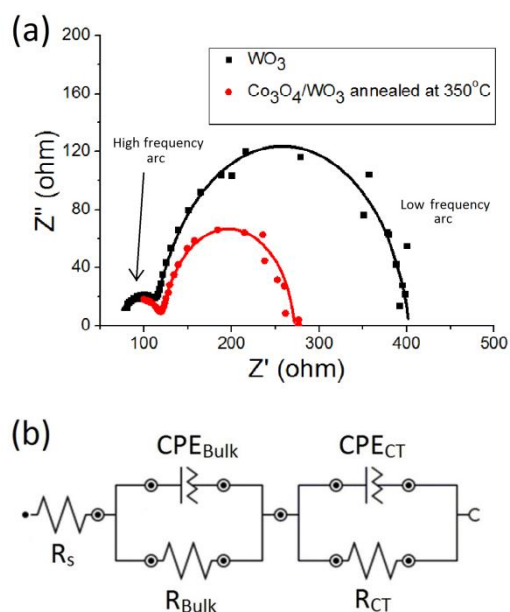**Figure 9** Energy band alignment diagrams for Co_3O_4/WO_3, Conduction and valence band edge positions of Co_3O_4 and WO_3 material are obtained from literature.[21, 22]

Figure 8 (a) Nyquist plot of electrochemical impedance spectroscopy data for WO_3 and Co_3O_4/WO_3 film annealed at 350 °C at 1.2V vs Ag/AgCl. (b) Equivalent circuit used for modelling the electrochemical cell. All capacitances are modelled using constant phase element (CPE) to achieve a good fitting. R_{Bulk} and CPE_{Bulk} refer to the resistance and capacitance across the bulk semiconductor while R_{CT} and CPE_{CT} correspond to the charge transfer interfacial layer between the electrode and the electrolyte.

Table 1 R_{Bulk}, CPE_{Bulk}, R_{CT}, CPE_{CT} values as obtained from electrochemical impedance spectroscopy simulation fit.

Samples	Cocatalyst annealing temperature (°C)	R_{Bulk} (Ω)	CPE_{Bulk} (μF)	R_{CT} (Ω)	CPE_{CT} (μF)
WO_3	-	49	1.10	284	55.8
Co_3O_4/WO_3	200	73	0.26	148	217
	300	52	0.28	172	138
	350	51	0.42	150	130
	400	43	0.55	139	126
	500	351	19.10	303	5.15

lower R_{CT} value shows that charge transfer is more efficient at the electrode/electrolyte interface with the incorporation of the cocatalysts, thus contributing to the enhanced photocurrent generated (Figures 6 and 7). This indicates good catalytic activity of the cocatalysts. In addition to the lower R_{CT} value, the charge transfer capacitance (CPE_{CT}) value is also found to be higher than bare WO_3 film. The charge transfer capacitance is related to the surface states, and a higher capacitance value indicates a greater surface density of states.[30] This finding is unsurprising, for amorphous materials are expected to have more unsaturated sites due to greater disorder in its structure.[31] Due to these unsaturated sites, a greater amount of water molecules can be adsorbed onto the film's surface,[32, 33] thus resulting in an increase in catalytic activity and photocurrent. The increase in surface states is also known to pin the Fermi level of the photocatalyst, and results in an anodic shift in the onset potential.[29] This offsets the
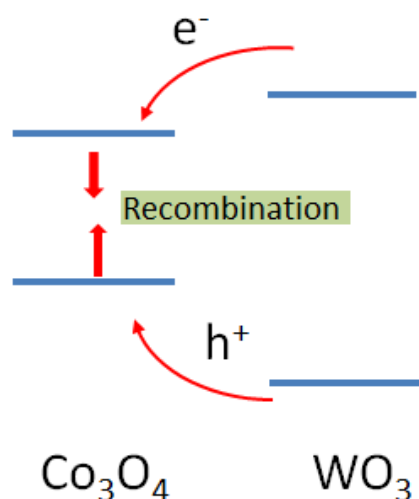
cathodic shift normally observed with the introduction of a cocatalyst, and may account for why only a marginal shift in onset potential has been observed (Figure 6). Another noteworthy trend is the decrease of R_{Bulk} as the cocatalyst annealing temperature increases from 200 °C to 400°C, which correlates nicely with the increasing trend of the photocurrent in this range of annealing temperatures (Figure 7). This may be explained by enhanced charge transport properties, due to reduced charge recombination as a result of the larger crystallite size of the cocatalyst film (as deduced from XRD data, Figure 2).

In comparison, the EIS data indicates significant increases in both R_{CT} and R_{Bulk}, and a huge decrease in CPE_{CT} value for highly crystalline cocatalysts annealed at 500 °C, corresponding to a significant decrease in photocurrent (Figure 7). The drop in CPE_{CT} is especially significant, from 126 μF to 5.15 μF when comparing cocatalysts annealed at 400 °C and 500 °C, respectively. The lower CPE_{CT} value shows that the highly crystalline cocatalyst has a lower density of lesser surface state while the higher R_{CT} indicates poorer charge transfer efficiency at the electrode/electrolyte interface. This corroborates with our earlier claim that highly crystalline cocatalysts exhibit lower density of unsaturated surface sites that are catalytically active. In addition to the decrease in surface sites, the increase crystallite size for Co_3O_4, as calculated using Scherrer's equation, also contributes to the poorer charge transfer properties due to a decrease in surface area.

On the other hand, the higher R_{Bulk} indicates inefficient charge transfer between the highly crystalline cocatalyst and WO_3 film. Indeed, the bulk resistance increases dramatically from 43 Ω to 351 Ω when comparing cocatalysts annealed at 400 °C and 500 °C. In order to understand this, we examined the band alignment between WO_3 and the cocatalyst. From Figure 9, which shows the relative conduction and valance
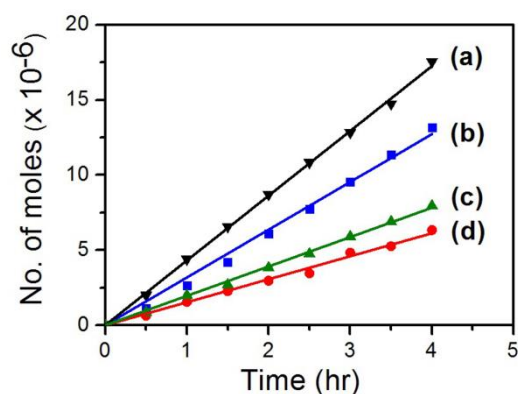
Figure 10 Hydrogen evolution under light illumination of (a) Co$_3$O$_4$/WO$_3$ and (b) WO$_3$. Oxygen evolution under light illumination of (c) Co$_3$O$_4$/WO$_3$ and (d) WO$_3$.

band edge positions of Co$_3$O$_4$ and WO$_3$ as obtained from literature,[21, 22] it can be seen that the Co$_3$O$_4$ cocatalyst forms unfavourable Type I heterojunction with WO$_3$ film. This encourages recombination of charge carriers upon charge transfer and can lead to high bulk resistance. It should be noted, however, that this is applicable only to highly crystalline materials that exhibit band transport and have well-defined energy bands. In contrast, charge transport in disordered amorphous semiconductors or nanocrystalline materials are typically described by a variable-range hopping model,[34] and thus are less affected by the effect of the unfavourable band alignment. We believe this is likely the reason for the increase in bulk resistance upon improvement in cocatalyst crystallinity. Thus, due to poorer charge transfer efficiency at the electrode/electrolyte interface and unfavourable energy band alignment of the cocatalysts with WO$_3$, the formation of crystalline cocatalyst film has a detrimental effect to the generated photocurrent.

Using amorphous Co$_3$O$_4$ annealed at 350 °C as the cocatalyst film, the H$_2$ and O$_2$ gas evolution rate from the water splitting process was measured. Figure 10 shows the H$_2$ and O$_2$ gas evolution of WO$_3$ and Co$_3$O$_4$/WO$_3$ film as a function of time. A linear gas evolution curve is observed which indicates that photocorrosion of the Co$_3$O$_4$/WO$_3$ did not take place. From the gradient of the gas evolution curve, bare WO$_3$ film shows a H$_2$ evolution rate of 3.2 µmol/h and an O$_2$ evolution rate of 1.5 µmol/h. This corresponds to a H$_2$:O$_2$ ratio of 2.13 which is close to the stoichiometry ratio of water splitting. On the other hand, Co$_3$O$_4$/WO$_3$ film has a higher gas evolution rate with its H$_2$ evolution rate at 34% higher than that of WO$_3$ film. The H$_2$ and O$_2$ evolution rate of Co$_3$O$_4$/WO$_3$ film is 4.3 µmol/h and 1.9 µmol/h respectively. From the amount of gas evolved and the measured photocurrent, the Faradaic efficiency of the reaction is calculated using Equation 3:[35, 36]

$$Faradaic\ efficiency = (n_{H2})/(Q/zF) \quad\quad (3)$$

where n_{H2} is the number of moles of hydrogen gas obtained, F is Faraday's constant (96,485 C/mol), Q is the total amount of charge passed through the cell, and z is the number of electrons transferred per hydrogen molecule (which is equal to 2). The total

number of moles of hydrogen obtained from a 4 hour illumination period is 17.3 µmol at an average photocurrent of 0.256 mA. Thus, $n_{H2} = 1.73 \times 10^{-5}$ mol and Q = 0.256 mA × 4 × 3600 s = 3.69 C. Plugging the above values into the equation, we obtained a high Faradaic efficiency of 90.0% for Co$_3$O$_4$/WO$_3$ film. This is a typical value for water splitting with PEC cell, and the less than unity efficiency can be explained by the back reaction occurring at the platinum counter electrode.[37] The gas evolution analysis confirms that the higher photocurrent led to higher gas evolution.

Conclusions

Co$_3$O$_4$ cocatalyst enhances the photocatalytic property of WO$_3$ at low annealing temperatures before the onset of crystallinity. The highest enhancement attained shows an increase of 40% in PEC property and 34% in H$_2$ gas evolution. The superior performance of Co$_3$O$_4$ is attributed to its excellent charge transfer property, from the photocatalyst to the electrolyte, which is indicative of high catalytic activity. The enhancement indicates the beneficial effects of an amorphous cocatalyst in improving the efficiency of photocatalytic water splitting process. At higher annealing temperatures, we conclude based on EIS data that the reduction of unsaturated active surface sites as well as mismatch of band structure between crystalline cocatalyst and WO$_3$ led to a deterioration of the generated photocurrent. These results help to explain the superior catalytic performance of amorphous cocatalyst, as well as elucidate the role played by cocatalysts in the photocatalytic water splitting process.

Acknowledgements

Notes and references

1. N. S. Lewis and D. G. Nocera, *Proc. Natl. Acad. Sci. U. S. A.*, 2006, **103**, 15729-15735.
2. M. G. Walter, E. L. Warren, J. R. McKone, S. W. Boettcher, Q. Mi, E. A. Santori and N. S. Lewis, *Chem. Rev.*, 2010, **110**, 6446-6473.
3. H. Dau, C. Limberg, T. Reier, M. Risch, S. Roggan and P. Strasser, *ChemCatChem*, 2010, **2**, 724-761.
4. R. Abe, M. Higashi and K. Domen, *ChemSusChem*, 2011, **4**, 228-237.
5. S. J. Hong, S. Lee, J. S. Jang and J. S. Lee, *Energy Environ. Sci.*, 2011, **4**, 1781-1787.
6. J. Kim, C. W. Lee and W. Choi, *Environ. Sci. Technol.*, 2010, **44**, 6849-6854.

7. A. B. Murphy, P. R. F. Barnes, L. K. Randeniya, I. C. Plumb, I. E. Grey, M. D. Horne and J. A. Glasscock, *Int. J. Hydrogen Energy*, 2006, **31**, 1999-2017.

8. J. Yang, D. Wang, H. Han and C. Li, *Acc. Chem. Res.*, 2013, **46**, 1900-1909.

9. T. K. Townsend, N. D. Browning and F. E. Osterloh, *Energy Environ. Sci.*, 2012, **5**, 9543-9550.

10. M. Higashi, K. Domen and R. Abe, *J. Am. Chem. Soc.*, 2012, **134**, 6968-6971.

11. S. Trasatti, *J. Electroanal. Chem.*, 1972, **39**, 163-&.

12. M. Bledowski, L. Wang, S. Neubert, D. Mitoraj and R. Beranek, *J. Phys. Chem. C*, 2014, **118**, 18951-18961.

13. D.-S. Lee, H.-J. Chen and Y.-W. Chen, *J. Phys. Chem. Solids*, 2012, **73**, 661-669.

14. K. Maeda, N. Saito, D. Lu, Y. Inoue and K. Domen, *J. Phys. Chem. C*, 2007, **111**, 4749-4755.

15. X. Zong, G. Wu, H. Yan, G. Ma, J. Shi, F. Wen, L. Wang and C. Li, *J. Phys. Chem. C*, 2010, **114**, 1963-1968.

16. M. Barroso, C. A. Mesa, S. R. Pendlebury, A. J. Cowan, T. Hisatomi, K. Sivula, M. Graetzel, D. R. Klug and J. R. Durrant, *Proc. Natl. Acad. Sci. U. S. A.*, 2012, **109**, 15640-15645.

17. M. W. Kanan and D. G. Nocera, *Science*, 2008, **321**, 1072-1075.

18. M. Barroso, A. J. Cowan, S. R. Pendlebury, M. Graetzel, D. R. Klug and J. R. Durrant, *J. Am. Chem. Soc.*, 2011, **133**, 14868-14871.

19. H. Dislich, *J. Non-Cryst. Solids*, 1985, **73**, 599-612.

20. J. Livage, M. Henry and C. Sanchez, *Prog. Solid State Chem.*, 1988, **18**, 259-341.

21. M. Long, W. Cai, J. Cai, B. Zhou, X. Chai and Y. Wu, *J. Phys. Chem. B*, 2006, **110**, 20211-20216.

22. D. W. Hwang, J. Kim, T. J. Park and J. S. Lee, *Catal. Lett.*, 2002, **80**, 53-57.

23. Q. Hao, D. Zhao, H. Duan and C. Xu, *ChemSusChem*, 2015, **8**, 1435-1441.

24. L. Lv, Y. Su, X. Liu, H. Zheng and X. Wang, *J ALLOY COMPD*, 2013, **553**, 163-166.

25. Y. Feng, L. Li, S. Niu, Y. Qu, Q. Zhang, Y. Li, W. Zhao, H. Li and J. Shi, *Appl. Catal., B*, 2012, **111**, 461-466.

26. J. Lin, P. Hu, Y. Zhang, M. Fan, Z. He, C. K. Ngaw, J. S. C. Loo, D. Liao and T. T. Y. Tan, *RSC Adv.*, 2013, **3**, 9330-9336.

27. W. Li, C. Liu, Y. Yang, J. Li, Q. Chen and F. Liu, *Mater. Lett.*, 2012, **84**, 41-43.

28. J. Yu, Y. Hai and M. Jaroniec, *J. Colloid Interface Sci.*, 2011, **357**, 223-228.

29. J. Zhao, E. Olide and F. E. Osterloh, *J. Electrochem. Soc.*, 2015, **162**, H65-H71.

30. X. Yang, C. Du, R. Liu, J. Xie and D. Wang, *J. Catal.*, 2013, **304**, 86-91.

31. J. F. Deng, H. X. Li and W. J. Wang, *CATAL TODAY*, 1999, **51**, 113-125.

32. D. Merki, S. Fierro, H. Vrubel and X. Hu, *Chem. Sci.*, 2011, **2**, 1262-1267.

33. U. Wolff, A. Gebert, J. Eckert and L. Schultz, *J ALLOY COMPD*, 2002, **346**, 222-229.

34. M. Grünewald and P. Thomas, *Phys. Status Solidi B*, 1979, **94**, 125-133.

35. C. G. Morales-Guio, S. D. Tilley, H. Vrubel, M. Graetzel and X. Hu, *Nature Communications*, 2014, **5**, 3059.

36. V. Perez-Herranz, M. Perez-Page and R. Beneito, *Int. J. Hydrogen Energy*, 2010, **35**, 912-919.

37. Y. Pihosh, I. Turkevych, K. Mawatari, T. Asai, T. Hisatomi, J. Uemura, M. Tosa, K. Shimamura, J. Kubota, K. Domen and T. Kitamori, *Small*, 2014, **10**, 3692-3699.

Electronic Supplementary Information

Effect of crystallinity on photocatalytic performance of Co$_3$O$_4$ water-splitting cocatalyst

Chin Sheng Chua,[a] Davide Ansovini,[a,b] Coryl Jing Jun Lee,[a] Yin Ting Teng,[d] Lay Ting Ong,[a] Dongzhi Chi,[a] T. S. Andy Hor,[a,c] Robert Raja,[b] and Yee-Fun Lim,[a]*

[a] Institute of Materials Research and Engineering (IMRE), A*STAR (Agency for Science, Technology and Research), 3 Research Link, Singapore 117602, Republic of Singapore.

[b] School of Chemistry, University of Southampton, Highfield, Southampton SO17 1BJ, United Kingdom.

[c] Department of Chemistry, National University of Singapore, 3 Science Drive 3, Singapore 117543, Singapore

[d] Energy Research Institute @NTU (ERI@N), Research Techno Plaza, X-Frontier Block, Level 5, 50 Nanyang Drive, Singapore 637553, Singapore

Email: limyf@imre.a-star.edu.sg
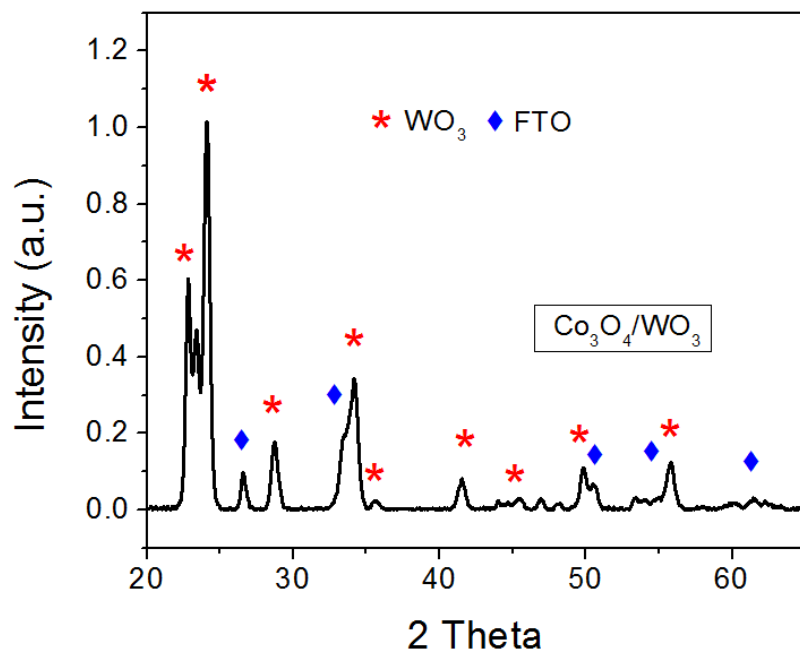
Figure S1. XRD spectra of 1 layer Co_3O_4 (annealed at 500 °C) on WO_3. Only WO_3 and FTO are detected, as the XRD is not sensitive enough to detect the ultra-thin Co_3O_4 layer.
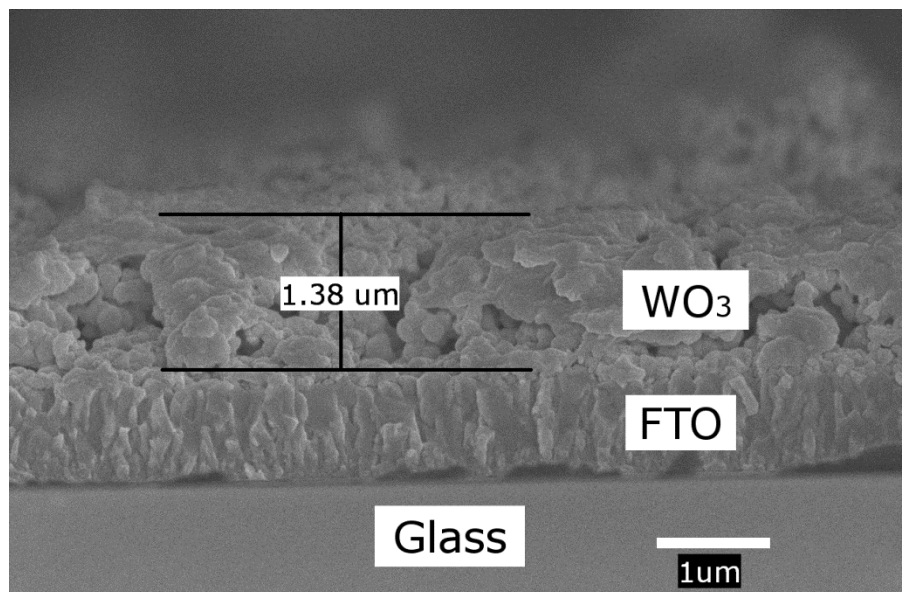

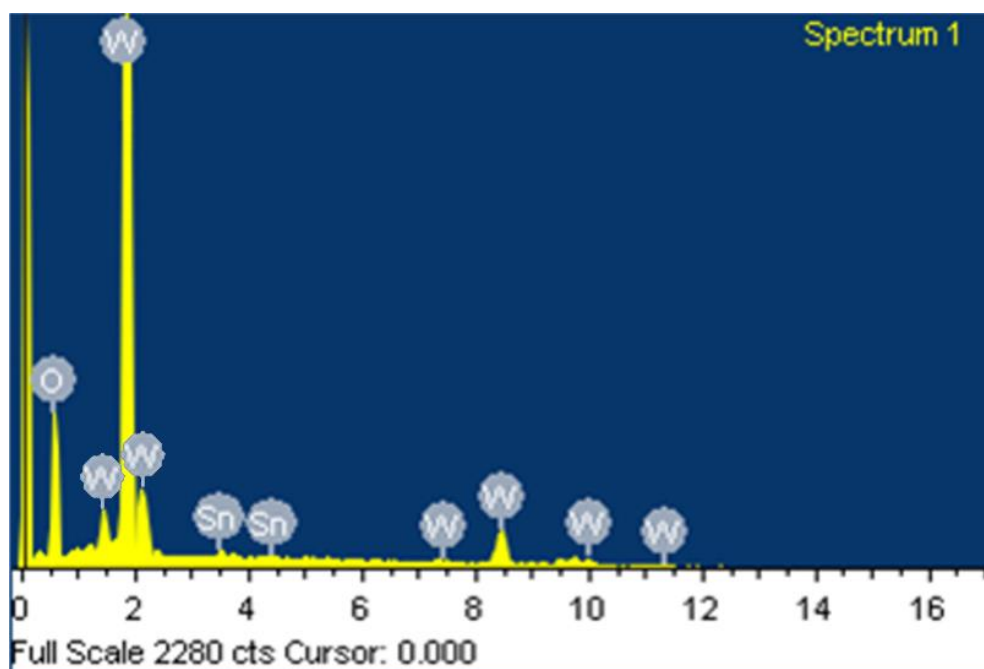
Figure S2. Cross-sectional view of Co_3O_4/WO_3 film

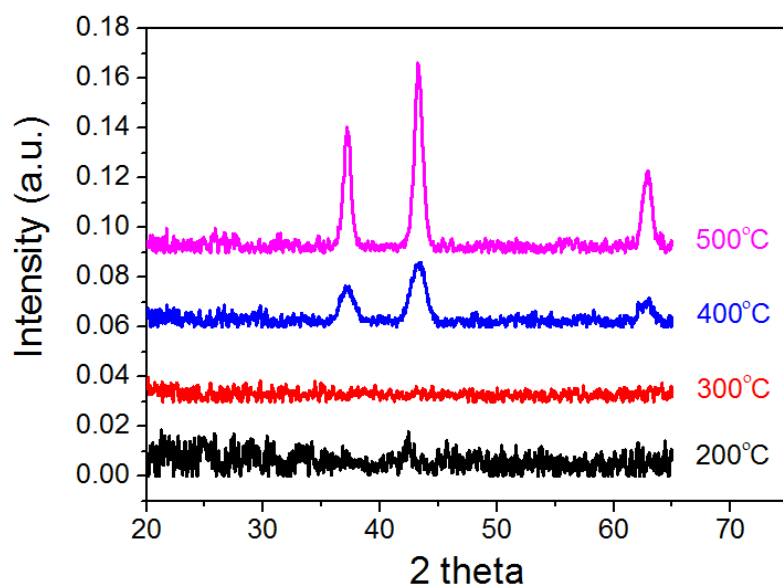**Figure S3.** EDX analysis of Co_3O_4/WO_3 film on FTO.

Figure S4. XRD spectra of NiO_x film on silicon at different annealing temperature.
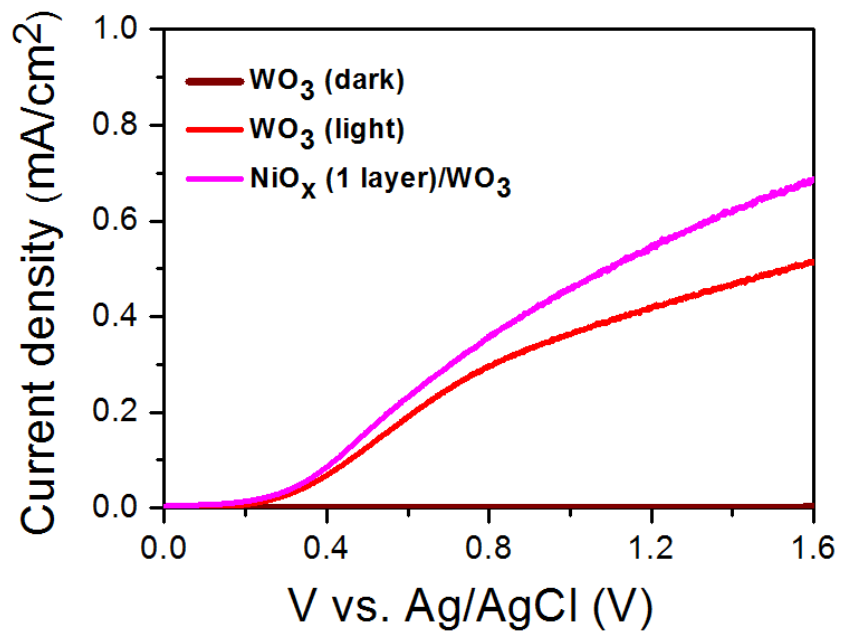
Figure S5. Photocurrent density of bare WO_3, and NiO_x/WO_3 (cocatalyst annealed at 350 °C).
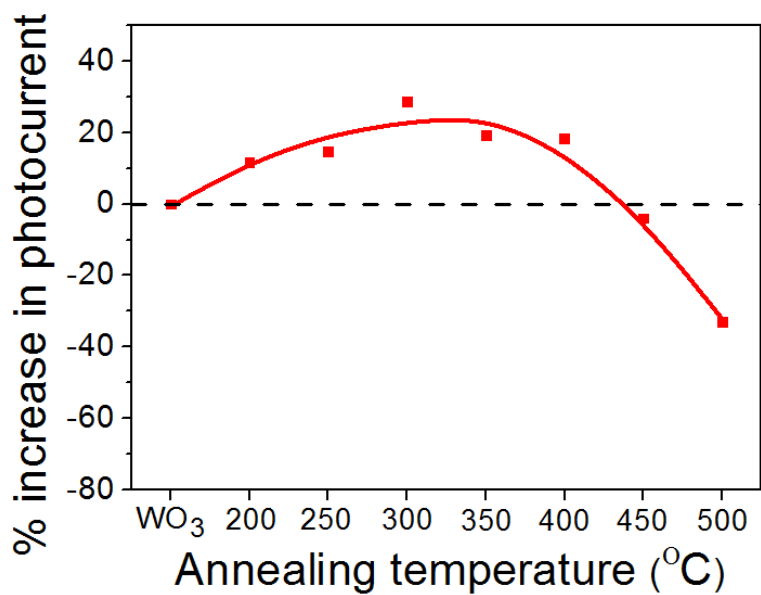

Figure S6. Percentage change in photocurrent (with respect to bare WO_3) with cocatalyst annealing temperature for NiO_x/WO_3 film at 1.2 V vs Ag/AgCl.